AGU PUBLICATIONS

JGR

Journal of Geophysical Research: Atmospheres

RESEARCH ARTICLE

10.1002/2016JD025896

Key Points:

- Comparison of simulations by using the Kain-Fritsch and Grell-Freitas schemes shows that the latter better captures U.S. summer precipitation
- Clouds and precipitation simulated by the Grell-Freitas scheme are less sensitive to model resolution than the Kain-Fritsch scheme
- The warm biases in the Southern Great Plains are related to large-scale circulation biases, which are insensitive to model resolution

Supporting Information:

- Supporting Information S1

Correspondence to:
L. R. Leung and Y. Gao,
ruby.leung@pnnl.gov;
yanggao@ouc.edu.cn

Citation:
Gao, Y., L. R. Leung, C. Zhao, and S. Hagos (2017), Sensitivity of U.S. summer precipitation to model resolution and convective parameterizations across gray zone resolutions, *J. Geophys. Res. Atmos.*, *122*, 2714–2733, doi:10.1002/2016JD025896.

Received 9 SEP 2016
Accepted 15 FEB 2017
Accepted article online 19 FEB 2017
Published online 8 MAR 2017
Corrected 24 AUG 2017

This article was corrected on 24 AUG 2017. See the end of the full text for details.

Sensitivity of U.S. summer precipitation to model resolution and convective parameterizations across gray zone resolutions

Yang Gao[1,2], L. Ruby Leung[1], Chun Zhao[1], and Samson Hagos[1]

[1]Atmospheric Sciences and Global Change Division, Pacific Northwest National Laboratory, Richland, Washington, USA,
[2]Now at College of Environmental Science and Engineering, Ocean University of China, Qingdao, China

Abstract Simulating summer precipitation is a significant challenge for climate models that rely on cumulus parameterizations to represent moist convection processes. Motivated by recent advances in computing that support very high-resolution modeling, this study aims to systematically evaluate the effects of model resolution and convective parameterizations across the gray zone resolutions. Simulations using the Weather Research and Forecasting model were conducted at grid spacings of 36 km, 12 km, and 4 km for two summers over the conterminous U.S. The convection-permitting simulations at 4 km grid spacing are most skillful in reproducing the observed precipitation spatial distributions and diurnal variability. Notable differences are found between simulations with the traditional Kain-Fritsch (KF) and the scale-aware Grell-Freitas (GF) convection schemes, with the latter more skillful in capturing the nocturnal timing in the Great Plains and North American monsoon regions. The GF scheme also simulates a smoother transition from convective to large-scale precipitation as resolution increases, resulting in reduced sensitivity to model resolution compared to the KF scheme. Nonhydrostatic dynamics has a positive impact on precipitation over complex terrain even at 12 km and 36 km grid spacings. With nudging of the winds toward observations, we show that the conspicuous warm biases in the Southern Great Plains are related to precipitation biases induced by large-scale circulation biases, which are insensitive to model resolution. Overall, notable improvements in simulating summer rainfall and its diurnal variability through convection-permitting modeling and scale-aware parameterizations suggest promising venues for improving climate simulations of water cycle processes.

1. Introduction

Dynamical downscaling has been used to advance understanding of regional climate processes [*Gao et al.*, 2012; *Hughes et al.*, 2007; *Leung and Ghan*, 1999; *Wang et al.*, 2004] and provide local-to-regional climate information for assessing climate impacts [e.g., *Mearns et al.*, 2015]. Regional climate models (RCMs) are common tools used in dynamical downscaling. RCMs simulate regional climate consistent with the boundary conditions, with the benefits of refined grid spacing to resolve regional processes that interact with the large-scale circulation. Increasing model resolution has been found to have the largest positive impacts on climate simulations in regions of complex terrain where increased grid resolution notably improves simulations of climate processes that are strongly influenced by orography [*Bacmeister et al.*, 2014; *Hughes and Hall*, 2010; *Leung and Qian*, 2003; *Leung et al.*, 2003; *Leung et al.*, 2004; *Rasmussen et al.*, 2011; *Zhang et al.*, 2009]. However, increasing model resolution does not invariably improve model skill. For example, correctly simulating the precipitation diurnal cycle has been a major challenge for both global and regional climate models. Climate models with a spatial resolution of 100 km or coarser generally produced summer peak precipitation 2 to 3 h earlier than observations over land, and increasing resolution to 30–50 km does not produce notable improvements [*Dirmeyer et al.*, 2012; *Jin et al.*, 2016; *Koo and Hong*, 2010].

In addition to model resolution, precipitation simulations are sensitive to the choice of cumulus parameterization, which can affect not only the occurrence and amount of precipitation but also the onset timing and location. *Dai et al.* [1999] tested three cumulus convection schemes, including Grell scheme [*Grell*, 1993], Kuo scheme [*Kuo*, 1974], and Zhang-McFarlane scheme [*Zhang and McFarlane*, 1995] at 60 km resolution and found that, in general, all three schemes failed to capture the broad spatial pattern of diurnal timing and amplitude of precipitation in the U.S., although the Grell and Kuo schemes captured most of the late afternoon to early morning precipitation peak over the Rockies and the eastern plain areas. Similarly, *Liang et al*. [2004] evaluated the summer precipitation diurnal cycle over the U.S. at 30 km resolution and found better performance of the Grell scheme over the Central Plains, but both the Grell and Kain-Fritsch schemes failed to reproduce the peak rainfall late afternoon timing in central Texas and the southeast. Evaluating simulations at 12 km grid resolution using 18 model configurations including the Kain-Fritsch and Betts-Miller-Janjić cumulus schemes as well as turning off the cumulus scheme, *Jankov et al*. [2005] did not find any single configuration that was clearly better than others.

In the Central U.S., mesoscale convective systems (MCSs) are the dominant sources of summer precipitation and a particular challenge for climate models and convection schemes. The diurnal timing of rainfall in the Great Plains is dominated by convection that develops in the Rocky Mountains during late afternoon and propagates toward the Great Plains [*Carbone et al*., 2002; *Davis et al*., 2003]. With moisture supplied by the nocturnal Great Plains low-level jet and favorable large-scale environments, the convective cells that are initiated in the mountains can organize into MCSs and contribute 30%–70% of the total warm-season precipitation in the Central U.S. [*Fritsch et al*., 1986; *Nesbitt et al*., 2006]. The typical dry biases and mid-to-late afternoon instead of nocturnal timing of peak rainfall in the Great Plains are likely symptomatic of the inability of climate models to represent MCSs. The resulting dry biases may amplify surface temperature biases as a response to the soil moisture deficits [*Klein et al*., 2006].

Recent advances in computing have enabled convection-permitting climate modeling, which explicitly resolves rather than parameterizes convection. This has enabled more skillful simulations of diurnal precipitation variability [*Ban et al*., 2014] and extreme precipitation [*Ban et al*., 2015; *Chan et al*., 2014; *Kendon et al*., 2012]. In addition to the Europe-based studies, *Clark et al*. [2009] found more accurate precipitation forecasts over the Central U.S. by using a regional model at 4 km resolution compared to that at 20 km. However, until very recently, computational limitations still constrained high-resolution convection-permitting RCMs to relatively small domains [*Prein et al*., 2015], so few studies have explored convection-permitting climate modeling over larger regions such as the conterminous U.S. [*Prein et al*., 2017].

Besides increasing model resolution, developing scale-aware parameterizations is an active area of research to address the longstanding model biases in simulating precipitation and other water cycle processes. Recognizing that traditional cumulus parameterizations developed for low-resolution models may not be appropriate for high-resolution models, scale-aware parameterizations are designed to adapt to a wide range of grid spacings, with the goal of improving model fidelity and reducing the sensitivity of model simulations to horizontal resolution. Scale-aware parameterizations are particularly important for RCMs and global variable resolution models [e.g., *Sakaguchi et al*., 2015], with computational domains spanning a wide range of resolutions through nesting and unstructured grids, respectively.

This study aims to investigate the sensitivity of RCM simulations to model resolution and the choices of cumulus parameterizations, which are closely related as the latter often display large sensitivity to model resolution. Such a sensitivity exploration has yet to be conducted at continental scale, as previous investigations were limited to small areas such as Central U.S. [e.g., *Clark et al*., 2009]. We focus on summer precipitation, particularly its diurnal variability, in the Central U.S. where MCSs play a key role in producing precipitation and its nocturnal timing. The Weather Research and Forecasting (WRF) model [*Skamarock et al*., 2008] is used at grid spacings ranging from 4 km to 36 km across the gray zone at which clouds and convective transport are partly resolved [*Shin and Hong*, 2013]. At the gray zone resolution (approximately between 4 km and 15 km), the model grid cell is too small to enable a statistical treatment of the collective effects of the cloud ensembles, which forms the basis of traditional cumulus parameterizations commonly used in climate models [*Arakawa et al*., 2011]. As 4 km may not span the high-resolution end of the gray zone, a shorter sensitivity simulation at 1 km grid spacing was also performed to explore model resolution sensitivity beyond 4 km.

We explore the scale awareness of convective parameterization schemes by comparing simulations with the Kain-Fritsch scheme, which is a traditional parameterization widely used in WRF, and the scale-aware Grell-Freitas scheme at resolutions of 4 km, 12 km, and 36 km. At this resolution range, we also compare simulations with hydrostatic (H) and nonhydrostatic (NH) dynamics, as their differences may be amplified as model resolution increases across the gray zone. More specifically, nonhydrostatic dynamics may produce noticeable improvement in simulating orographic precipitation [*Janjić et al*., 2001]. As dynamics interact with the moist physics, the impacts of using H versus NH dynamical cores could be non-negligible even at mesoscale

Table 1. WRF Simulation Experiments for the Summer (June-July-August (JJA)) of 2006 and 2007

	36 km		12 km		4 km	
	Cumulus Scheme	Nonhydrostatic	Cumulus Scheme	Nonhydrostatic	Cumulus Scheme	Nonhydrostatic
KF_NH	KF	Yes	KF	Yes	N/A[a]	Yes
KF_H	KF	No	KF	No	N/A	No
GF_NH	GF	Yes	GF	Yes	GF	Yes
SPEC NUDGE_UV_KF			KF	Yes		
SPEC NUDGE_UV_GF			GF	Yes		

[a]N/A, not applicable.

resolutions [*Yang et al*., 2017]. Additional simulations performed by using spectral nudging are also used to further explore the relative impacts of large-scale circulation biases on simulations of precipitation. In what follows, we describe the model configuration and sensitivity experiments in section 2. An analysis of the simulations is discussed in section 3, and the study is summarized with discussion in section 4.

2. Model Configuration and Sensitivity Experiments

2.1. Model Configuration

The Weather Research and Forecasting model (WRF) version 3.5.1 is used in this study. To evaluate the impacts of grid spacing, an identical domain covering the continental U.S. and the surrounding land and ocean areas is used for simulations at 36 km, 12 km, and 4 km resolution. All simulations used lateral boundary conditions and sea surface temperatures from the North American Regional Reanalysis (NARR) at 32 km resolution [*Mesinger et al*., 2006]. The domain center is set at 38.5°N and 96°W, with a model top at 100 hPa and 35 vertical layers. Physics options including the Morrison double-moment microphysical scheme [*Morrison et al*., 2009], the Mellor-Yamada-Janjić planetary boundary layer (PBL) scheme [*Janjić*, 1990; *Mellor and Yamada*, 1982], the Rapid Radiative Transfer Model for GCMs shortwave and longwave radiation scheme [*Iacono et al*., 2008; *Morcrette et al*., 2008], and the unified Noah land surface model [*Chen and Dudhia*, 2001; *Ek et al*., 2003] are used.

We performed continuous simulations from 1 April to 31 August of 2006 and 2007 and analyzed only the summer period (June, July, and August). We selected 2006 and 2007 because the contrasting dry and wet conditions over the Southern Great Plains may allow a more robust evaluation of model sensitivity to grid resolutions and convection schemes. The Southern Great Plains is an important region as it is frequented by MCSs that dominate the diurnal variability of rainfall that challenges climate modeling. The two relatively extreme climatic conditions were driven largely by differences in large-scale circulation [*Dong et al*., 2011] that can be reasonably captured by the NARR boundary conditions.

2.2. Sensitivity Experiments

We use a matrix of simulations to compare the effects of nonhydrostatic versus hydrostatic dynamical cores and two cumulus schemes: the Kain-Fritsch (KF) scheme [*Kain*, 2004] and the scale-aware Grell-Freitas (GF) scheme [*Grell and Freitas*, 2014] at three grid spacings (36 km, 12 km, and 4 km), except that for KF, the parameterization is turned off at 4 km convection-permitting resolution. Recent development of the Grell-Freitas convection scheme [*Grell and Freitas*, 2014] as an update of the Grell-Dévényi scheme [*Grell and Dévényi*, 2002] improves scale awareness by introducing the method of *Arakawa et al*. [2011] to relax the assumption of traditional convective parameterizations that convection is contained within individual model grid column when the fractional area covered by convection clouds is small. Across the gray scales, many of the assumptions in the traditional convective parameterizations are no longer valid. Ideally, a scale-aware scheme should converge to an explicit simulation of cloud processes as model resolution increases [*Grell and Freitas*, 2014].

Table 1 summarizes the simulations analyzed in this study. The simulation domains cover the same geographic extent (Figure S1a in the supporting information) but include different number of grid cells depending on the grid resolution (see Figures S1b–S1d for the grid structure at 4 km, 12 km, and 36 km resolutions). Boundary conditions were applied to a width consisting of five grid points including a boundary buffer zone of four grid points in each simulation domain. The impacts of nudging are only evaluated with simulations at 12 km grid spacing. Two types of nudging technique are available in WRF to constrain the model simulations toward the observed or analyzed weather conditions. While analysis nudging adds a nudging tendency term proportional to the difference between the simulated and the reanalyzed/observed states [*Stauffer and Seaman*, 1990], spectral nudging applies a nudging term as an interior forcing in the spectrally transformed equations of states [*von Storch et al*., 2000; *Waldron et al*., 1996]. Both grid nudging and spectral nudging simulations were conducted with comparable results, so only results from spectral nudging are shown. Nudging was applied only to the vertical layers above the PBL to constrain the large-scale circulation, with a nudging coefficient of $3 \times 10^{-4}\,s^{-1}$ [*Stauffer and Seaman*, 1990]. A wave number of three was selected in both south-north and west-east directions, corresponding to length scales of about 1000 km and 1800 km, respectively. A sensitivity test using a wave number of five in the west-east direction for comparable length scales in the north-south direction and west-east direction yielded similar results. Except for tests designed to evaluate nonhydrostatic effects, all simulations used the nonhydrostatic dynamical core. For the same grid spacing, the computational times for simulations with different cumulus schemes (or without a cumulus scheme) and hydrostatic versus nonhydrostatic dynamical cores are indistinguishable. Using 160 cores on a Cray XC30 with a peak performance of 2.57 petaflop/s, 1 day of simulation on average takes about 20 min of wall clock time at 4 km grid spacing and 8 min at 12 km grid spacing over the conterminous U.S.

3. Analysis of Simulations

3.1. Seasonal Mean Surface Air Temperature and Precipitation

3.1.1. Evaluation of Surface Air Temperature

Figure 1 shows the mean bias in seasonal mean 2 m air temperature simulated for the summers of 2006 and 2007 compared to a 0.125° resolution gridded data set based on observations (OBS) from surface stations [*Maurer et al*., 2002]. Quantitative model performance is shown in Figure 2 by using Taylor diagrams [*Taylor*, 2001], where the radial distance from the origin indicates the standard deviations of both models (σ_f) and observations (σ_r) normalized by the observational standard deviation σ_r, so it is equal to 1.00 for the observation, shown as the thick dashed line in Figure 2. The correlation coefficient (R) is given by the angular coordinate. The root-mean-square difference (E), normalized by the standard deviation of the reference data, is reflected by the radial distance between the reference (*REF*) point and another point such as a WRF simulation, indicated by the thin dashed circle centered at the reference point in Figure 2. The root-mean-square difference E is computed based on the equation shown below [*Taylor*, 2001]. The mean percentage bias relative to observation is also indicated by the circles or the triangles in different sizes as indicated in Figure 2 (top left).

$$E^2 = {\sigma_f}^2 + {\sigma_r}^2 - 2\sigma_f\sigma_r R$$

Figures 1 and 2 show relatively small temperature biases generally within 2°C of the observed values. The spatial correlations between WRF and OBS are 0.8 or higher for all cases, reflecting fairly good agreement in terms of spatial distribution. Larger warm biases of about 4–5°C are found in the Southern Great Plains with both KF and GF. These warm biases are somewhat reduced in the 4 km simulations. Simulations with hydrostatic dynamics have somewhat larger warm biases. Interestingly, the biases in the Great Plains are dramatically reduced in simulations with nudging at 12 km grid spacing compared to all other simulations regardless of resolution. This point will be discussed further in section 3.3.

3.1.2. Evaluation of Seasonal Mean Precipitation

A 0.125° observational data set [*Maurer et al*., 2002] based on daily rain gauge data with topographic adjustment of the monthly precipitation from the PRISM data [*Daly et al*., 1994] is used for comparison with model simulations. For simulations without nudging (Figures 3d–3l), there is a general wet bias east of the Rockies and dry bias over the Southern Great Plains. The performance at 36 km and 12 km is comparable (Figures 3d, 3g, and 3j versus Figures 3e, 3h, and 3k), but a strong improvement at 4 km compared to 12 km and 36 km is clear (i.e., Figures 3f, 3i, and 3l versus Figures 3e, 3h, and 3k). In particular, compared to the 36 km and 12 km simulations, the 4 km simulations (Figure 4a) show smaller normalized standardized variation (close to 1) and higher spatial correlation of 0.6 to 0.7. Comparing the simulations with the KF and GF cumulus schemes, the GF scheme shows much smaller bias at both 36 km (Figure 3g versus Figure 3d) and 12 km (Figure 3h versus Figure 3e) grid spacings, and the 4 km simulations with the GF scheme (Figure 3i) are comparable to the 4 km simulations without cumulus scheme (Figure 3f). Focusing on the simulations with GF, the mean bias (Figures 3g–3i) and spatial correlation (Figure 4a) of the 36 and 12 km simulations are comparable to that of the 4 km simulations, albeit larger normalized variance in the 36 km and 12 km simulations. This result

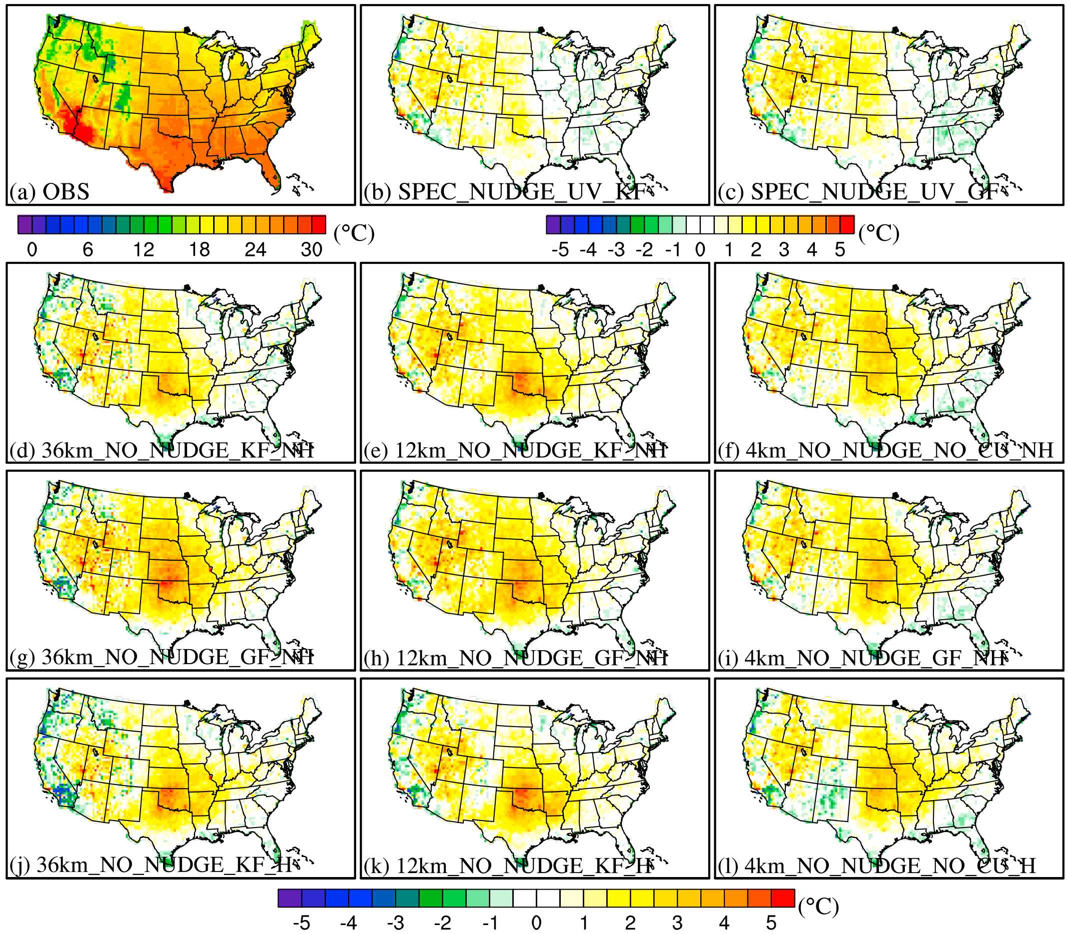

Figure 1. (a) Spatial distribution of seasonal mean temperature from observations and the (b) mean bias from the WRF simulations averaged over the summers of 2006 and 2007 in °C. For the WRF simulations, cases with spectral nudging are denoted as SPEC_NUDGE_UV (nudging U and V only at 12 km grid spacing) and cases without nudging are denoted as NO_NUDGE. Notations are also used to differentiate simulations with the KF (Kain-Fritsch), GF (Grell-Freitas), or no (NO_CU) convective parameterization schemes and simulations at different grid spacings (36 km, 12 km, and 4 km). See Table 1 for more details of the specifications of the WRF simulations.

suggests that precipitation simulated by the GF scheme is less sensitive to model resolution, as expected from the scale awareness in the design of the parameterization.

The WRF simulations with hydrostatic and nonhydrostatic dynamical cores perform similarly in terms of the spatial distribution of model biases (Figures 3g–3i versus Figures 3j–3l) and spatial correlation (Figure 4a, case 1 versus case 3). However, simulations with nonhydrostatic dynamics notably reduce the large wet bias in the Rocky Mountains and Sierra Nevada, particularly at 36 km (Figure 3g versus Figure 3j) and 12 km (Figure 3h versus Figure 3k) when a convection scheme is used. Hence, the nonhydrostatic simulations show higher correlation for all three (36 km, 12 km, and 4 km) spatial resolutions compared to the hydrostatic simulations. This is consistent with *Lebassi-Habtezion and Diffenbaugh* [2013], who also found that nonhydrostatic simulations more accurately resolve the spatial heterogeneity of surface climate associated with topography in the western U.S. It is interesting to note that the reduction of wet biases extends to the Northern Great Plains east of the Rocky Mountains at all three resolutions. This may be an indication of the effects of nonhydrostatic dynamics on the gravity waves excited by orographic forcing in the Rocky Mountains that propagate to the Great Plains and influence clouds and precipitation there. Also, consistent with *Yang et al.* [2017] who noted the importance of physics-dynamics interactions in amplifying the difference between simulations with hydrostatic versus nonhydrostatic dynamical cores, our results show larger differences between H and NH at 36 km and 12 km resolution with the KF scheme compared to 4 km resolution without a cumulus scheme.

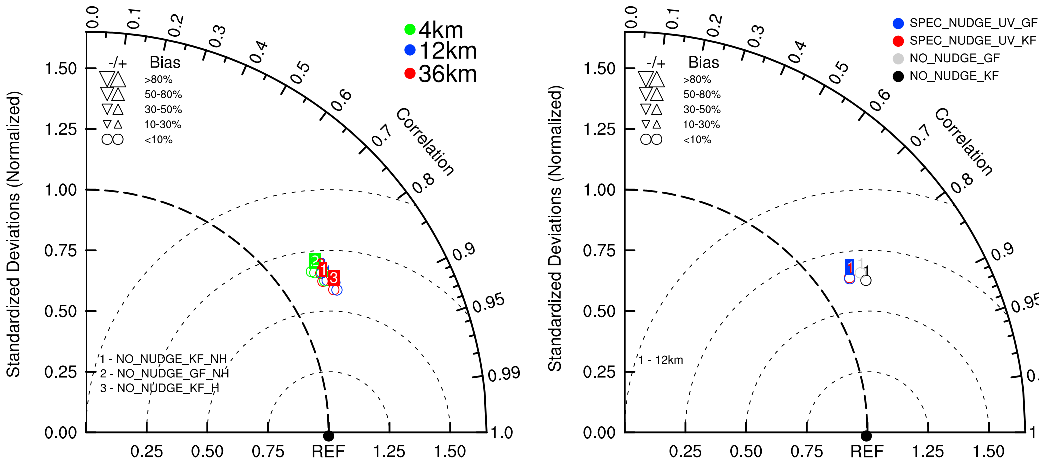

Figure 2. Taylor diagrams of spatial statistics of the summer mean (JJA in 2006/2007) 2 m temperature for the WRF simulations relative to observations. Three statistical metrics including the normalized standard deviation (radial coordinate), the spatial correlation coefficient (angular coordinate), and the normalized root-mean-square difference (radial distance between the reference point (black dot on *x* axis) and the data point) are displayed. Different colors and symbols are used to distinguish the various simulations following the notations described in Figure 1.

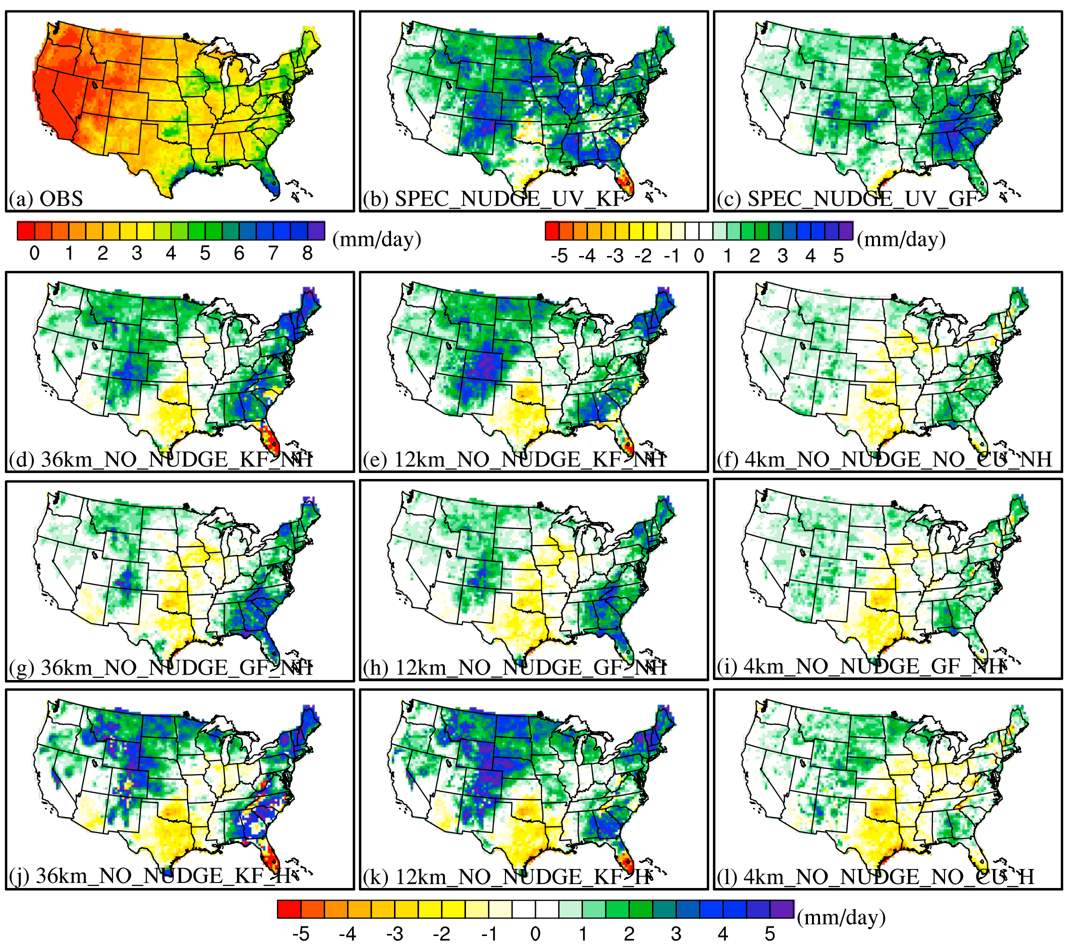

Figure 3. Same as Figure 1 but for the seasonal mean precipitation in mm/d.

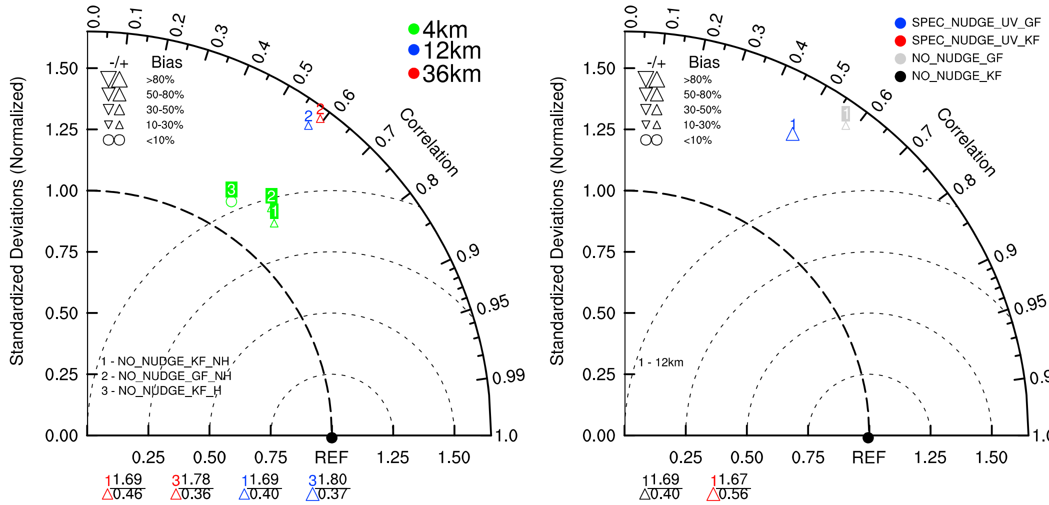

Figure 4. Same as Figure 2 but for the spatial statistics of the summer mean (JJA in 2006/2007) precipitation.

In comparing the nudging and no nudging cases, a reduction of the dry bias over the Southern Great Plains in the nudging simulations is apparent. However, simulations with nudging still produced too much precipitation over New Mexico, Colorado, and the southeast at 12 km grid spacing, similar to cases without nudging (Figure 3e). Overall, from Figure 4b, nudging improves the spatial correlation (i.e., 0.56 with nudging versus 0.40 without nudging for KF), but the percentage bias and standardized variance are similar to those without nudging. The wet bias over New Mexico and Colorado is largely reduced at 4 km grid spacing (Figures 3f, 3i, and 3l) and 12 km by using GF (Figure 3h). However, the dry bias in the Southern Plains and Texas is rather insensitive to model resolution (Figures 3d–3f versus Figures 3g–3i), but with nudging, the dry bias is largely alleviated. More detailed analyses of the precipitation biases will be discussed in section 3.3.

3.2. Diurnal Cycle of Precipitation

3.2.1. Comparison Across River Basins

To investigate how different WRF configurations perform in terms of the diurnal cycle of precipitation, the continental U.S. is divided into 12 river basins. Four WRF simulations are compared in Figure 5. Three observational data sets featuring subdaily precipitation derived from different data sources at different spatial resolutions are used for comparison. The first data set, Precipitation Estimation from Remote Sensing Information using Artificial Neural Network (PERSIANN), provides hourly precipitation data at a spatial resolution of 0.25° × 0.25° from 60°S to 60°N [*Hsu et al.*, 1999; *Sorooshian et al.*, 2000]. The second data set, the Tropical Rainfall Measuring Mission (TRMM) produced by the 3B-43 algorithm, also has a spatial resolution of 0.25° × 0.25° but at a three hourly temporal resolution and covers 50°S to 50°N [*Huffman et al.*, 2001; *Huffman et al.*, 2007]. The last data set is hourly precipitation data from the North American Land Data Assimilation System (NLDAS) on a 0.125° × 0.125° grid over North America [*Xia et al.*, 2012a; *Xia et al.*, 2012b]. The NLDAS precipitation is generated from rain gauge data with topographic adjustment by using the PRISM data set, combined with Doppler Stage II radar precipitation data.

The observational data (black lines and stars in Figure 5) are generally comparable in both diurnal amplitude and peak hour of precipitation, despite some differences. The timings of the peak precipitation are within 1 h among the three data sets over a majority of river basins, except for a larger discrepancy in North Central (NC) river basin (Figure 5c). The magnitude of precipitation also depicts a good agreement, except for the tendency of PERSIANN to show larger peak values in some basins (i.e., Figures 5f, 5g, and 5j–5l). The moderate discrepancy has been reported by *Liang et al.* [2004], who noted differences of 2–3 h in peak precipitation over the central Rockies and southeast between rain gauge measurement and multisensor analysis data. The WRF simulations at 4 km (blue line in Figure 5) without cumulus parameterization can be considered a reference case since they yield the best performance in terms of both spatial distributions and correlations shown in Figures 3 and 4. As shown in Figure 5, the 4 km simulations capture the diurnal cycle, particularly

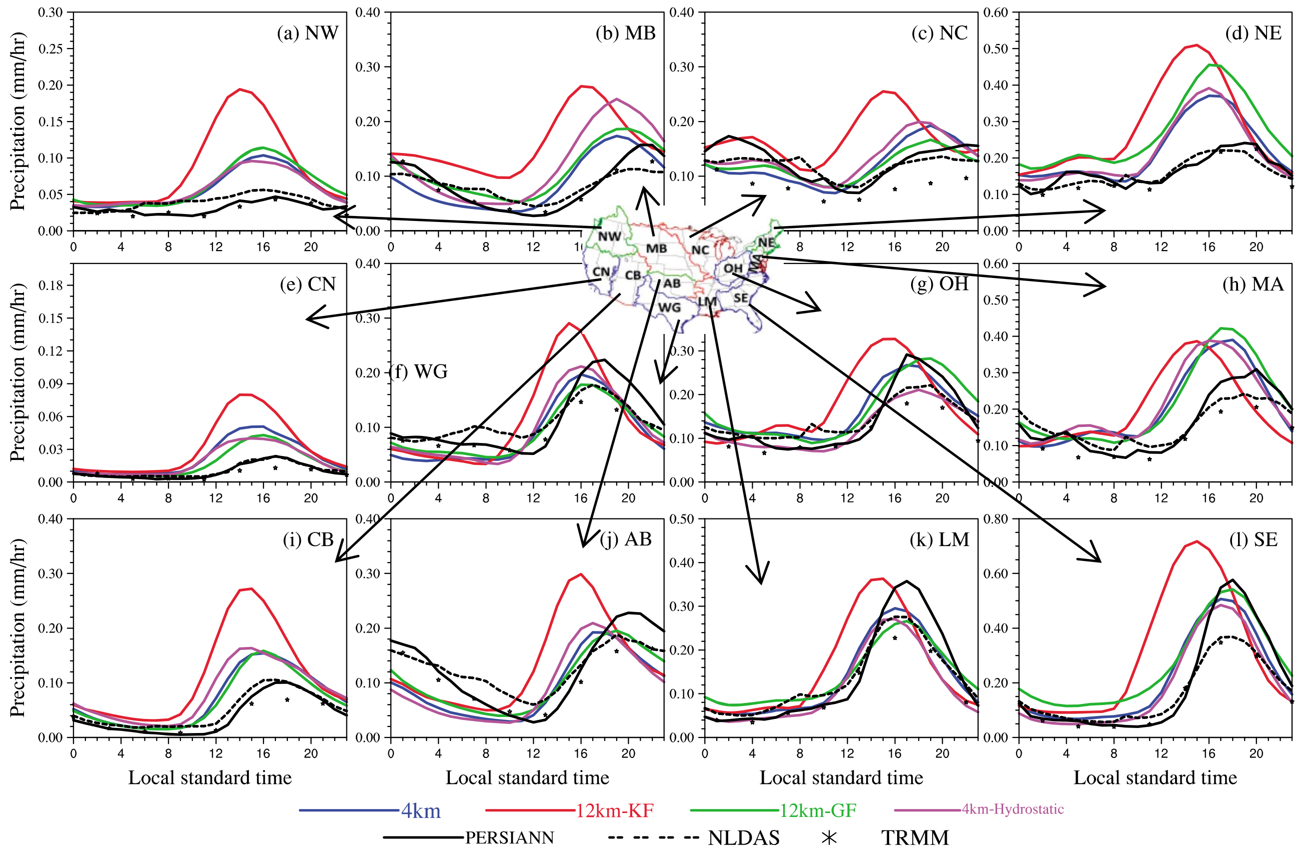

Figure 5. Diurnal cycle of precipitation for the two-summer mean of 2006 and 2007. The four simulations are all performed without nudging. Observations from PERSIANN, NLDAS, and TRMM are shown in black, while simulations are shown in colors: The blue and magenta colors indicate simulations at a grid spacing of 4 km with no convection scheme, with nonhydrostatic and hydrostatic dynamics, respectively, and the red and green colors indicate simulations at a grid spacing of 12 km, with nonhydrostatic dynamics and the KF and GF convection schemes, respectively. The conterminous United States is divided into 12 river basins (http://www.nws.noaa.gov/geodata/catalog/hydro/html/rfcbounds.htm) (AB: Arkansas-Red Basin, CB: Colorado Basin, CN: California-Nevada, LM: Lower Mississippi, MA: Middle Atlantic, MB: Missouri Basin, NC: North Central, NE: northeast, NW: northwest, OH: Ohio, SE: southeast, WG: West Gulf).

the timing of the peak precipitation such as the nocturnal peak in the Great Plains and late afternoon peak in most other locations fairly well. In contrast, the 12 km simulations with the KF scheme (red lines) consistently produce peaks that are 1 to 4 h earlier than the 4 km simulations and the observational data sets and precipitation is also too strong. The 36 km simulations produce similar biases as the 12 km simulations, which is consistent with an earlier study [*Liang et al.*, 2004, Figure 2] evaluating 30 km simulations by using the KF scheme. We conducted two 1 month simulations for June 2007 at 12 km resolution by using the KF scheme to test two variants of the trigger function that add temperature perturbation of the convective parcel based on (1) moisture advection and (2) relative humidity [*Ma and Tan*, 2009]. Consistent with previous studies that experimented with the trigger function in different convection schemes [e.g., *Bechtold et al.*, 2014; *Hohenegger and Stevens*, 2013], the simulations show only minor differences in the diurnal timing of rainfall (not shown).

When KF is replaced by GF in the 12 km simulations (green lines), both the diurnal peak and mean precipitation are comparable to those of the 4 km simulations, except for some larger positive biases such as over northeast (NE; Figure 5d) and southeast (SE; Figure 5l). A previous study found that biases in precipitation timing were reduced over the Central Plains in the Grell cumulus scheme in comparison to the KF scheme, but the biases were still large in the Southern Great Plains and southeast (5–10 h earlier than observations, as shown in *Liang et al.* [2004, Figures 2e and 2f]). From our results, the 4 km simulations with hydrostatic and nonhydrostatic dynamics produce similar performance, with differences of 1 or 2 h for peak precipitation over a few river basins (northwest (NW), NC, California-Nevada (CN), Middle Atlantic (MA), and Colorado Basin (CB) at Figures 5a, 5c, 5e, 5h, and 5i). This similarity between nonhydrostatic and hydrostatic dynamical core with respect to diurnal variability also applies to the 12 km and 36 km simulations. With the GF scheme,

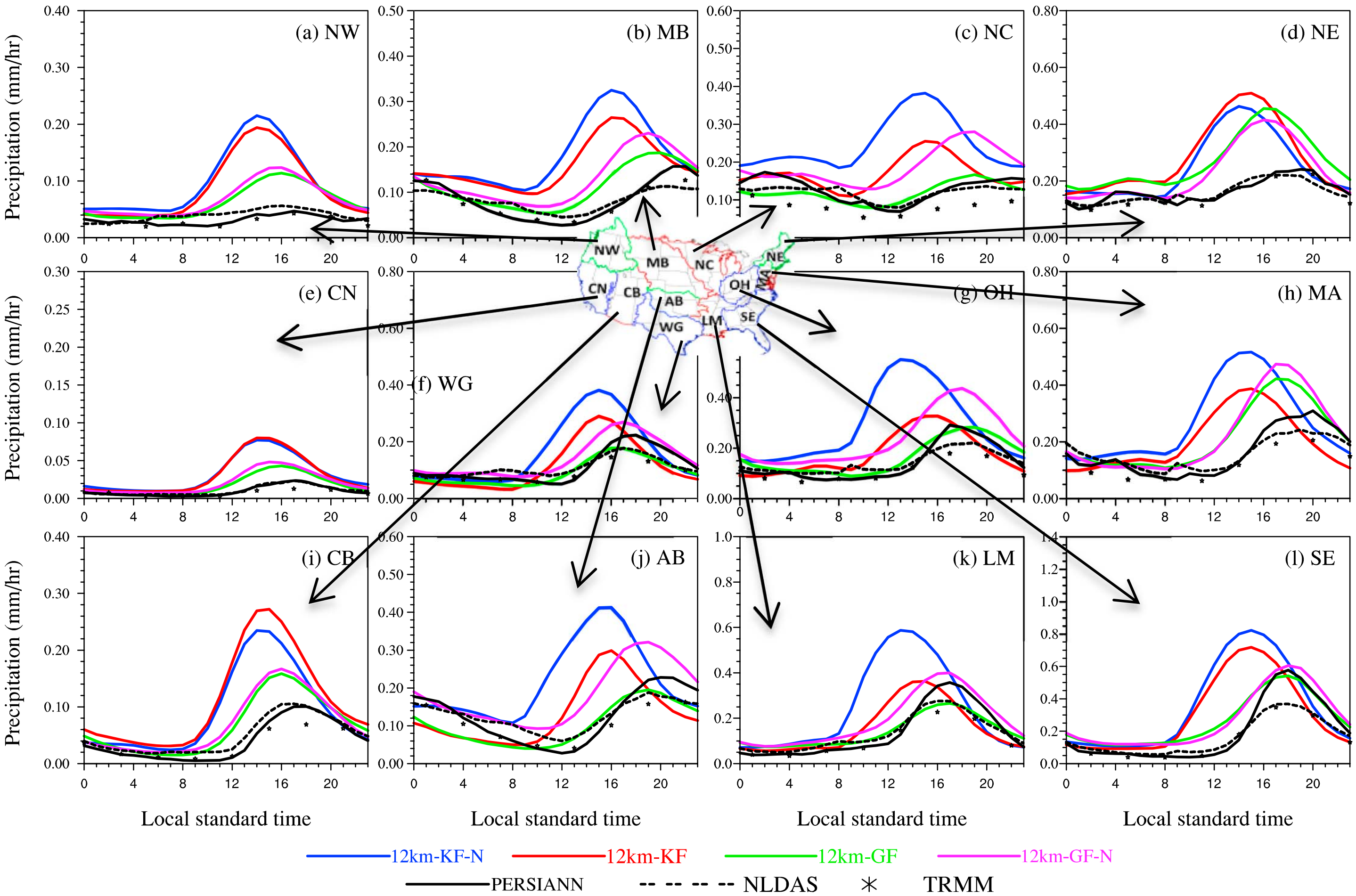

Figure 6. Same as Figure 5 comparing simulations with (12 km KF-N and 12 km GF-N) and without (12 km KF and 12 km GF) nudging at a grid spacing of 12 km.

both the 4 km and 12 km simulations are comparable to the 4 km simulations without cumulus scheme, in terms of both mean and peak precipitation. This provides further evidence of reduced sensitivity of the GF scheme to model resolution.

To examine whether the improvements at 4 km grid spacing, regardless of the cumulus schemes, are related to the ability to better resolve topography or the ability to explicitly simulate convection, a sensitivity test was conducted for the summer of 2006 (not shown). While keeping all settings the same, we replaced the 4 km topography with that used in the 12 km simulations. We found very small impacts of the smoothed topography on either the timing or magnitude of diurnal precipitation. This suggests that the improved precipitation at 4 km compared with 12 km is mainly associated with the explicit simulation of convection.

The diurnal cycle of the 12 km WRF simulations with and without nudging is shown in Figure 6. Overall, these simulations for the same physics parameterizations do not exhibit notable differences in the diurnal timing, but the diurnal amplitude could differ, consistent with the changes in seasonal mean precipitation. This indicates that nudging and nonhydrostatic dynamics may improve the seasonal mean and spatial distribution of precipitation (Figure 3), but they have little effect on simulating diurnal timing of precipitation. Similar conclusions can be drawn from simulations with both the KF and GF schemes with and without spectral nudging.

3.2.2. Diurnal Precipitation in the Great Plains and North American Monsoon Regions

Tian et al. [2005] documented the strong spatial variations of diurnal rainfall amplitude and phase in North America, highlighting the role of topography, land-sea contrast, and coastline curvature in modulating the diurnal cycle. To further investigate the impacts of model resolution and cumulus parameterization on diurnal rainfall, the magnitude of precipitation maxima (diurnal amplitude) and timing of precipitation maximum (diurnal phase) are analyzed in two regions, the Great Plains and North American monsoon, both exhibiting

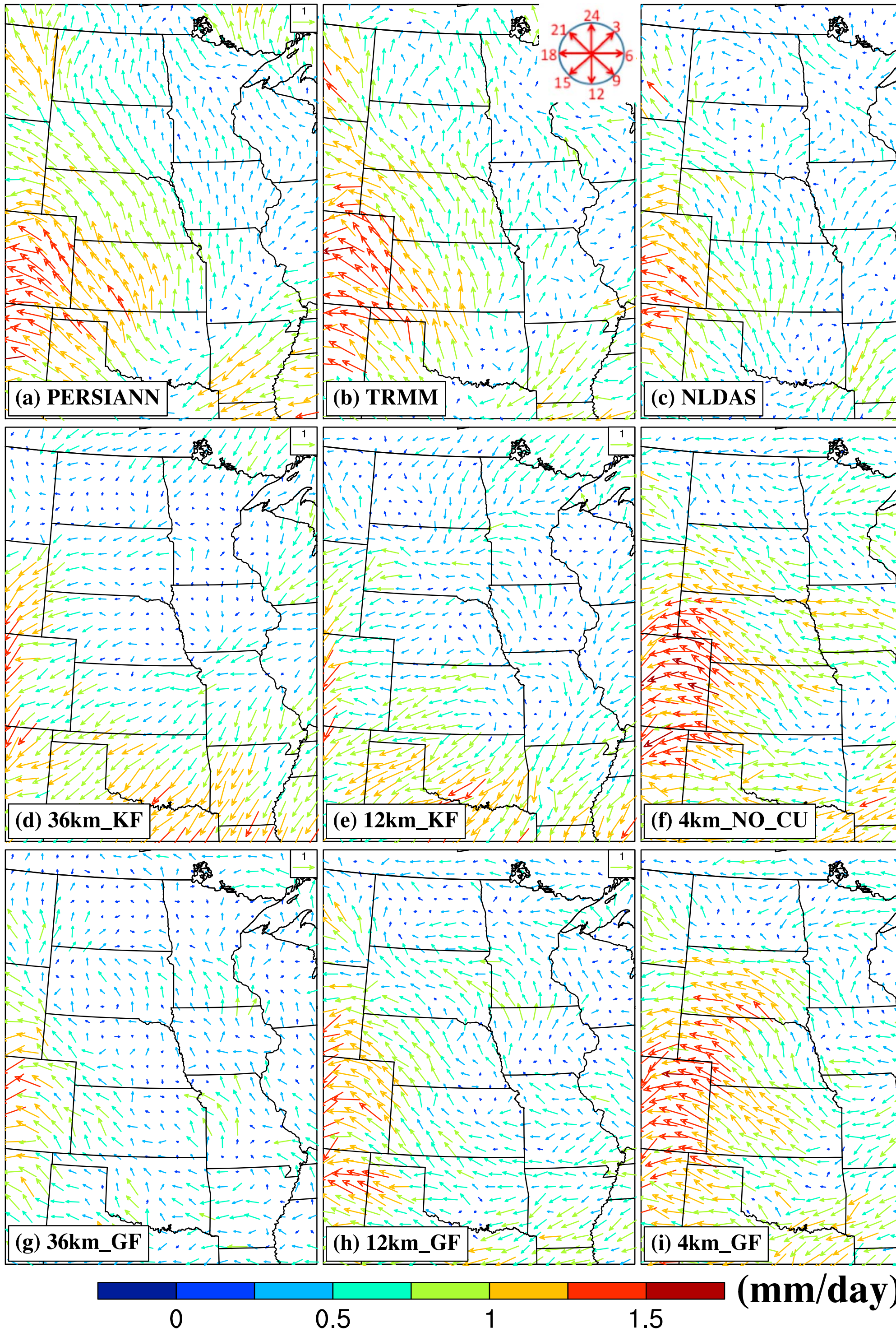

Figure 7. Diurnal cycle of precipitation over the Great Plains, with the length/color and direction of the arrows indicating the magnitude of precipitation maxima in mm/d and timing of precipitation maximum in local standard time, respectively. Observations are shown at the top for the PERSIANN, TRMM, and NLDAS data sets. For simulations, the grid spacing and convection scheme used in each simulation is indicated in the label of each panel.

distinct features of diurnal variability. The diurnal amplitude and phase of the first diurnal harmonic are calculated by using Fourier analysis on hourly (or 3 hourly for TRMM) precipitation averaged over the 2006 and 2007 summers. The diurnal amplitude and phase are shown as vectors in Figures 7 and 8.

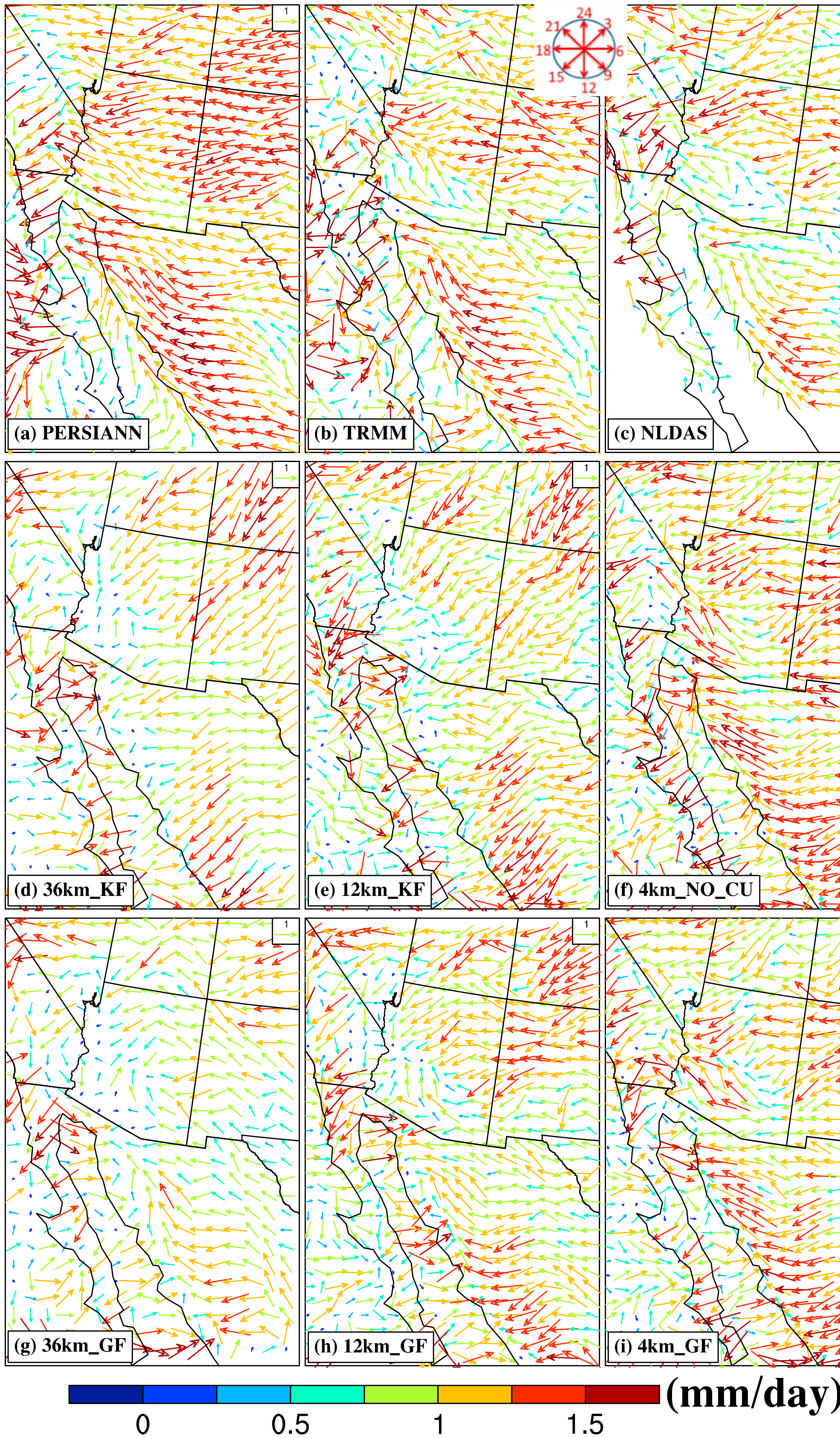

Figure 8. Same as Figure 7 but for the North American monsoon region.

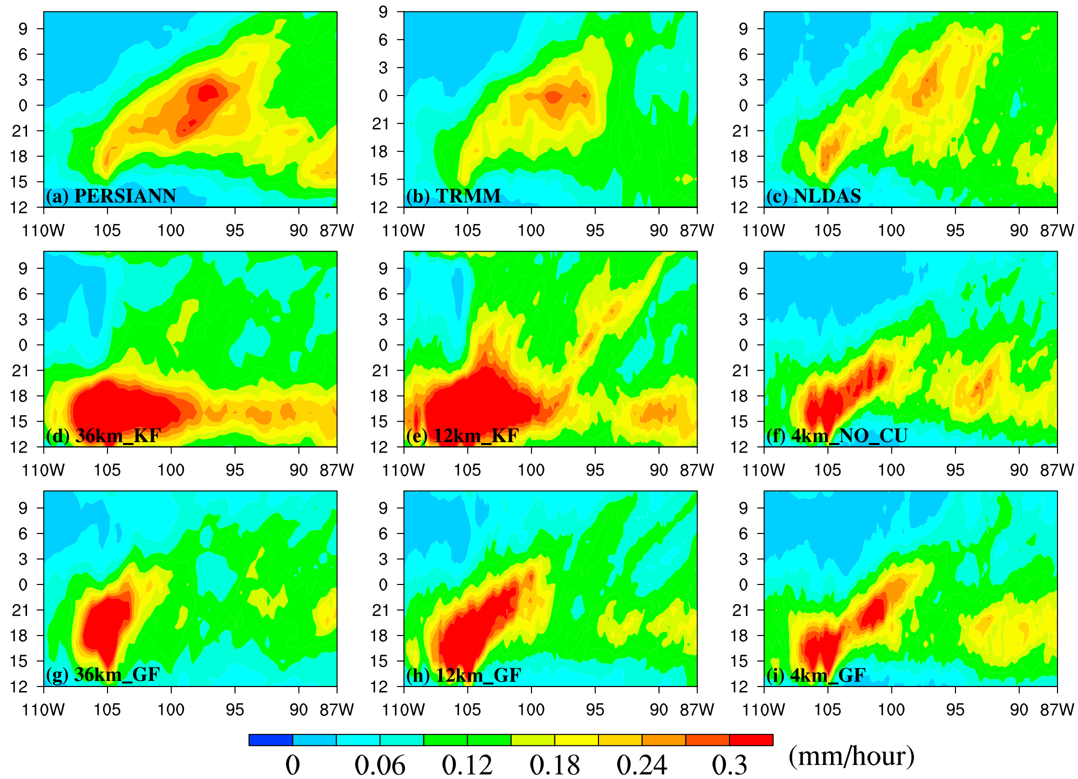

Figure 9. Hovmöller diagrams of precipitation diurnal variations averaged over 36°–42°N in the Great Plains at local standard time shown in the *y* axis for (top row) three observational data sets and (middle and bottom rows) different WRF simulations. All simulations are run without nudging.

The three observational data sets (Figures 7a–7c) agree with each other on the diurnal phase and amplitude, illustrating a dominant nocturnal peak around 21:00 local standard time (LST) in the southern and central Great Plains. This nocturnal timing shifts to a late afternoon (18:00 LST) peak and a midafternoon (15:00 LST) peak transitioning from the plains to the Rocky Mountains and the southeast, respectively. These features are satisfactorily reproduced by the 4 km simulations without a cumulus scheme (Figure 7f) and the 12 km and 4 km simulations with the GF scheme (Figures 7h and 7i). Interestingly, even at 36 km grid spacing, the GF simulations captured the observed diurnal phase much better than the 36 km and 12 km simulations with the KF scheme, which produced peak precipitation more synchronous with the maximum surface heating in midafternoon.

In the North American monsoon region (Figure 8), there is a clear transition from a late afternoon peak in the Sierra Madre and Rocky Mountains to a nocturnal peak west of the mountains in the three observational data sets (Figures 8a–8c). This spatial pattern is well captured by the 4 km simulations without cumulus scheme and simulations with the GF cumulus scheme at all spatial resolutions (36 km, 12 km, and 4 km). Similar to the Great Plains area, the precipitation at 36 km and 12 km with the KF scheme shows earlier peaks that are on average 3–4 h earlier compared to the observations.

3.2.3. Eastward Propagation of Cloud and Precipitation

Figure 9 shows Hovmöller diagrams of hourly or three-hourly precipitation averaged over 36°–42°N. All three observational data sets (Figures 9a–9c) clearly show the eastward propagation of summer convective systems initiated at the Rockies (between 100°W and 105°W) in late afternoon. The propagating feature is generally consistent among the three observations, although the magnitude varies, with PERSIANN showing higher peak precipitation. This broad feature is largely captured by the WRF simulations at 4 km without cumulus parameterization (Figure 9f) and the 36 km, 12 km, and 4 km WRF simulations with the GF scheme (Figures 9g–9i), although the propagating feature in the 36 km simulations is limited to west of 100°W. When the KF scheme is used, precipitation occurs predominantly between noon and early afternoon across the Great Plains at 36 km (Figure 9d), and even at 12 km (Figure 9e), only very weak propagation can be discerned.

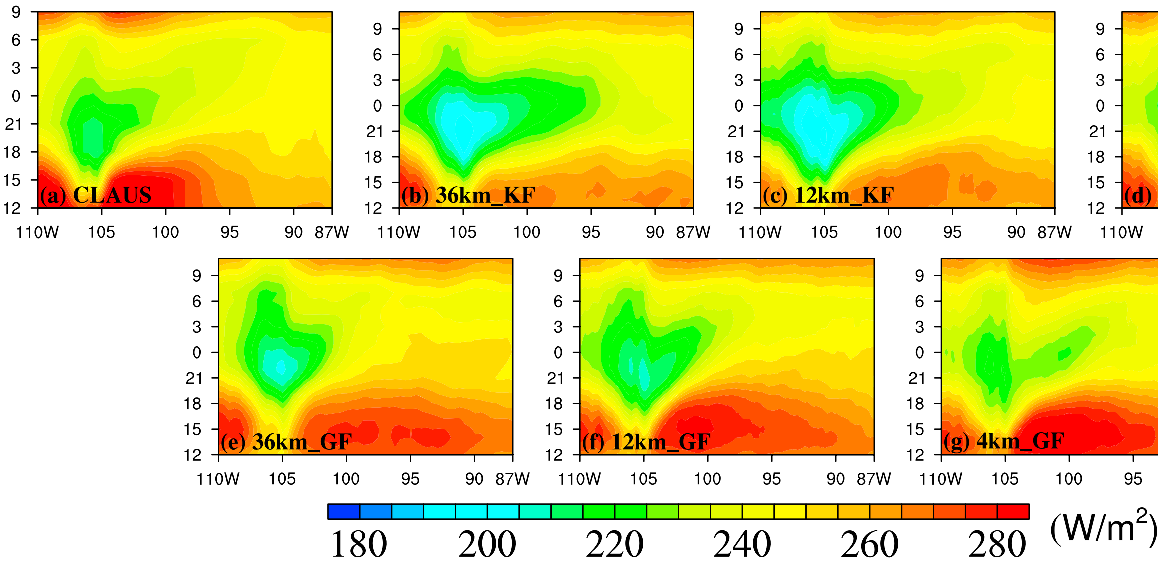

Figure 10. Outgoing longwave radiation from (a) CLAUS and (b–g) WRF simulations averaged over 36°–42°N at local standard time shown in the *y* axis. All WRF simulations in this figure are run without nudging.

The propagation of convection in the Great Plains can also be clearly observed from the outgoing longwave radiation derived from the half-degree global 3-hourly brightness temperature (T_b) (11–12 μm) from Cloud Archive User Service (CLAUS) [*Hodges et al.*, 2000; *Yang and Slingo*, 2001]. The diurnal cycle of outgoing longwave radiation depicted in Figure 10 resembles the precipitation feature shown in Figure 10, showing deep convective clouds propagating eastward from 105°W to 95°W between 18:00 and 3:00 LST (Figure 10a). This feature is well captured by the 4 km simulations without cumulus scheme and simulations with the GF scheme at all three resolutions (36 km, 12 km, and 4 km). With the KF scheme, convection is too strong for both 36 km and 12 km, with outgoing longwave radiation on average 20 W/m^2 lower than the observation. In contrast, the cloud top in the GF simulations is more comparable with the observation. There is a tendency for the cloud top to lower with increasing resolution in GF, but the KF cloud top height shows little sensitivity to resolution or even slightly higher cloud top at 12 km than 36 km. Lastly, in KF, the highest cloud top occurs between 18:00 and 00:00 LST, although precipitation peaks between noon and 21:00 LST. Hence, precipitation in simulations with the KF scheme is generated mostly before the onset of deep convection. In contrast, more of the precipitation in the GF simulations is associated with deeper convective clouds.

3.2.4. Resolution Sensitivity of the KF and GF Schemes

Our analysis of seasonal mean and diurnal precipitation clearly shows improved simulation skill and reduced sensitivity of the GF scheme to model resolution compared to the KF scheme. These results are summarized in Figure 11 for comparisons of simulations by using KF and GF in the Southern Great Plains. At grid spacing of 36 km and 12 km, the KF scheme produces a dominant peak in diurnal precipitation at 3 P.M. LST. The daily mean precipitation changes by 18% from 0.16 mm/h to 0.13 mm/h from 36 km to 12 km grid spacing. In contrast, the GF scheme produces a diurnal peak at midnight LST at all three resolutions. The 4 km GF simulation is very similar in both diurnal timing and amplitude to the 4 km simulation with no convective scheme. Also noticeable, the GF simulations are much less sensitive to resolution changes, showing almost no change in daily mean precipitation across the three resolutions.

Since convective parameterization likely dominates the behavior of diurnal precipitation in the WRF simulations, we compare the diurnal variability of the ratio of large-scale (resolved) precipitation to the total precipitation (Figure 11b). This ratio is simply equal to one for the 4 km simulation with no convective parameterization. For the 36 km KF simulation, this ratio is smaller than 0.2 throughout the day, with a small peak at 8 A.M. LST. This indicates that most precipitation is produced by the KF scheme at 36 km grid spacing and the parameterization is more active between noon and 8 P.M. LST when nearly all precipitation is produced by the KF scheme. At 12 km grid spacing, the ratio of large-scale to total precipitation shows more diurnal variability, with the KF scheme less active compared to the 36 km simulation in

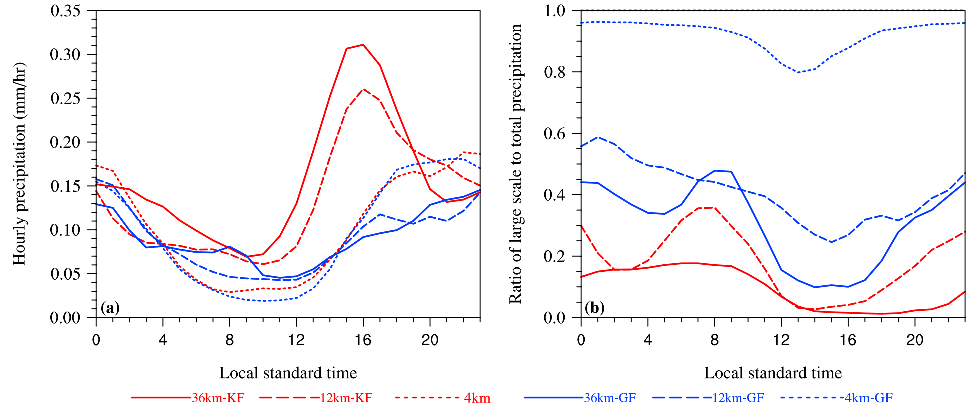

Figure 11. Comparisons of mean diurnal variations in the central Great Plains (in Kansas State) of (a) hourly precipitation (mm/h) and (b) the ratio of large-scale to total precipitation in simulations using the KF and GF convection schemes at grid spacings of 36 km, 12 km, and 4 km. The KF scheme is turned off at 4 km grid spacing.

the morning (5 to 11 A.M.) and late afternoon and evening (4 P.M. to 1 A.M.) hours. So as resolution increases, more precipitation is produced by large-scale precipitation than parameterized convection, leading to an overall reduction of daily mean precipitation and a reduced dominance of the afternoon peak at 12 km compared to 36 km. However, these changes are not sufficient to shift the diurnal peak away from the afternoon because KF produces over 95% of the total precipitation between 1 and 5 P.M. at both 12 km and 36 km.

The ratio of large-scale to total precipitation is substantially larger in the GF simulations than the KF simulations at both 12 km and 36 km. So the GF scheme plays a less dominating role in generating precipitation and produces lower cloud top compared to the KF scheme (Figure 10). Interestingly, the diurnal variation of this ratio in GF at 36 km (solid blue) is similar to that of KF at 12 km (red dashed). Hence, the GF scheme is also most active between noon and 4 P.M. at 36 km grid spacing, but it produces only 85 to 55% of the total precipitation between 4 P.M. and midnight, respectively, so the diurnal precipitation has a midnight peak. With increasing resolution to 12 km, the peak at 8 A.M. disappears and the GF scheme produces less than 50% of the total precipitation at all times. Further increasing resolution to 4 km dramatically reduces the contribution of the GF scheme to the total precipitation to less than 20%. Hence, once again, the GF scheme manifests scale awareness, as it produces proportionately less precipitation and lower cloud top as model resolution increases, providing a gradual transition across the gray scale and reducing the overall sensitivity of the total precipitation to resolution.

To further compare the resolution sensitivity of the KF and GF schemes, two 1 month simulations in June 2007 were conducted at 4 km grid spacing with the KF scheme and no convective scheme. The simulation produces a peak precipitation timing comparable to that simulated at 4 km without the KF scheme. This result demonstrates the larger sensitivity of the KF scheme to model resolution compared to the GF scheme across the gray zone resolutions. Lastly, to explore the resolution sensitivity at the higher resolution end of the gray zone, two 1 month simulations (June 2007) were conducted over a large area of the U.S. (Figure S2) at the grid spacing of 1 km and 4 km. From Figure S3 the diurnal precipitations simulated at 4 km and 1 km resolution, both without a cumulus parameterization, are comparable, with similar diurnal timing of maximum and minimum rainfall. This suggests that the model is capable of resolving deep convection reasonably at 4 km resolution.

3.3. Impacts of Nudging on Surface Temperature Biases

As noted from Figure 1, warm biases in the Southern Great Plains, particularly over northern Texas and Oklahoma, are apparent in simulations without nudging. These biases are largely reduced with spectral nudging of the winds above the PBL (Figure 1b). These results provide an opportunity to examine the warm biases that are not only most prominent in the lower resolution simulations but also noticeable in the 4 km simulations. Figure 12 shows the differences of 2 m air temperature and precipitation between the KF simulations with and without spectral nudging at a grid spacing of 12 km. Surface temperature with

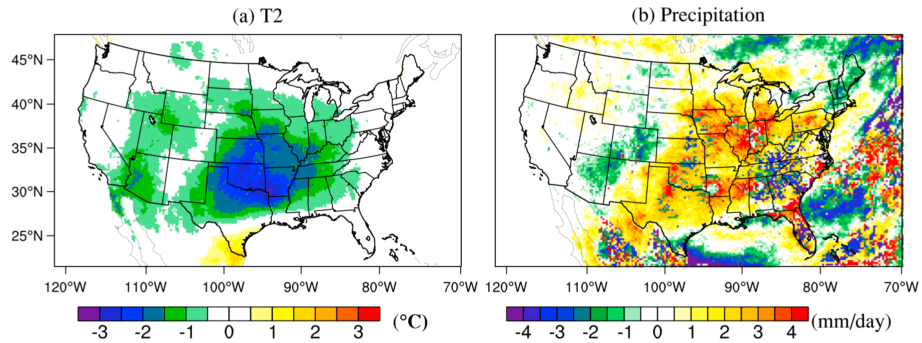

Figure 12. Differences of (a) 2 m air temperature and (b) precipitation between simulations with and without spectral nudging at a grid spacing of 12 km.

nudging is up to 3°C lower than the simulation without nudging, which corresponds well spatially with the higher precipitation over the same region. The enhanced precipitation with nudging substantially increases the latent heat flux, which is largely balanced by a reduction in the sensible heat flux corresponding to the reduced surface temperatures.

To understand how nudging induces changes in precipitation that reduce the warm surface temperature biases, we perform a moisture budget analysis on the simulations with and without nudging. The moisture budget can be expressed as follows:

$$\rho g(P - E) = -\nabla \int_0^{P_s} qVdP \tag{1}$$

In equation (1), P is precipitation, E is evaporation, ρ is the density of water, and $\nabla \int_0^{P_s} qVdP$ is the divergence of vertically integrated moisture flux. Following *Seager et al*. [2010], we express the differences of $P - E$ between the two simulations as

$$pg\delta(P - E) = -\delta\left(\nabla \int_0^{P_s} qVdP\right) \approx -\int_0^{P_s} \delta q \nabla VdP - \int_0^{P_s} \delta V \nabla qdP - \int_0^{P_s} \nabla \delta \nabla \ \delta qdP \tag{2}$$

The three terms on the right side of equation (2) are the thermodynamical effect (TH) due to difference of the mean moisture, the dynamical effect (DY) due to difference of the mean wind, and the transient effect (TR) due to covariation between the differences in mean moisture and mean wind, respectively. These budget terms comparing the simulations with and without nudging are shown in Figure 13. The total moisture divergence differences (Figure 13a) resemble the differences in P (Figure 12b) because the evaporation differences are generally very small compared to the P differences. The total moisture divergence differences are mainly contributed by the dynamical effects related to the differences in mean flow (Figure 13c), while the thermodynamical effects due to differences in the mean moisture (Figure 13b) are largely balanced by the transient covariation effects (Figure 13d), particularly in the southwest, Kansas, and the southeast. Thus, spectral nudging increases the moisture flux convergence over the southern Plains by altering the mean winds, which leads to enhanced precipitation.

To determine how the mean flow modulates the moisture flux convergence and precipitation in the spectral nudging case, Figure 14 shows the vertically integrated moisture and moisture flux for the base case (Figure 14a) and the differences between the two simulations (with/without nudging; Figure 14b). The model simulates high moisture in the Gulf of Mexico and Gulf of California with the warm sea surface temperatures in the summer. Associated with the North Atlantic subtropical high pressure system, the model captures the southeasterly wind bringing moisture from the Gulf of Mexico to the Southern Great Plains. With spectral nudging, moisture flux from the Gulf of California is enhanced (Figure 14b), which increases moisture flux convergence in the Southern Great Plains. Thus, the warm biases in the Southern Great Plains are partly related to the model biases in large-scale circulation and the resulting biases in moisture flux convergence and precipitation. Such biases affect simulations at all resolutions and are only alleviated by nudging of the winds. However, nudging has no effect on diurnal precipitation, while reducing the grid spacing to 4 km alleviates model biases in diurnal precipitation.

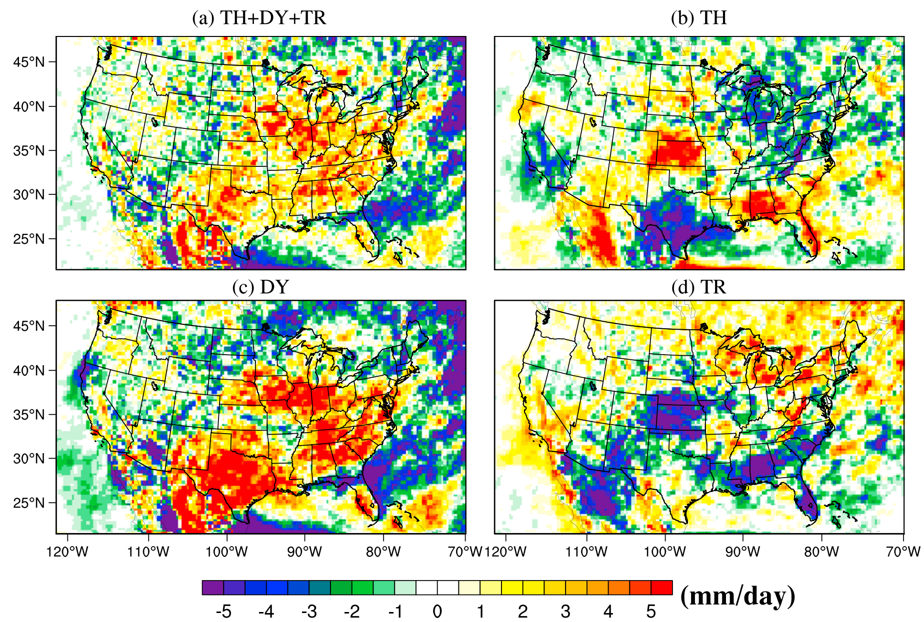

Figure 13. Moisture budget differences between simulations with and without spectral nudging for (a) differences in moisture flux divergence and the contributions to the moisture flux divergence from (b) thermodynamical effect (TH) due to differences of the mean moisture, (c) dynamical effect (DY) due to differences of the mean wind, and (d) transient effect (TR) due to the covariation between the differences in mean moisture and mean wind.

4. Summary and Discussions

In this study, a series of WRF simulations were conducted to document the sensitivity of regional climate simulations to spatial resolution ranging from mesoscale to convection-permitting scale. We focus on precipitation in a set of simulations over the conterminous U.S. at grid spacings of 36 km, 12 km, and 4 km. Along with the resolution sensitivity, we also investigate model sensitivity to convective parameterizations and nonhydrostatic versus hydrostatic dynamics, which are critical issues for modeling across the gray zone resolutions. Simulations with and without nudging of large-scale tropospheric winds provide an opportunity to evaluate the impacts of large-scale circulation biases on precipitation and surface temperature in regional climate simulations. As far as summer precipitation is concerned, the convection-permitting simulations at 4 km grid spacing are most skillful in reproducing the observed spatial distributions and the diurnal variability associated with eastward propagation of cloud and precipitation systems across the Great Plains. Consistent with *Lebassi-Habtezion and Diffenbaugh* [2013] and *Yang et al.* [2017], nonhydrostatic dynamics has a positive impact on precipitation simulations over the western U.S. with complex terrain even at

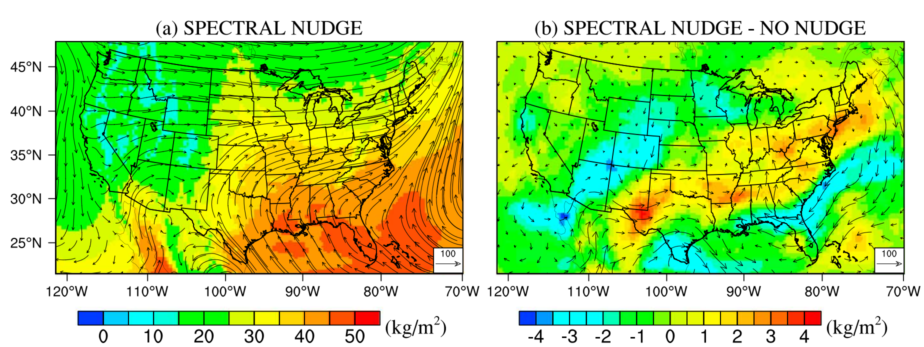

Figure 14. (a) Vertically integrated moisture (shading) and moisture flux (vector) for the spectral nudging case (SPECTRAL NUDGE) and the (b) differences of moisture (shading) and moisture flux (vector) due to the mean flow between simulations with and without spectral nudging.

12 km and 36 km grid spacings. The smaller differences between simulations with the hydrostatic versus nonhydrostatic dynamical core in this study compared to those in *Lebassi-Habtezion and Diffenbaugh* [2013] are likely related to the different emphases on precipitation in the warm versus cold seasons. Further, through physics-dynamics coupling, differences in physics parameterizations used in the two studies may lead to different response to the nonhydrostatic dynamics as well.

Precipitation in simulations at coarser resolutions is evidently more phase locked diurnally with the solar radiation induced surface heating, while observations show a more variable diurnal timing across the conterminous U.S. Notable differences are found between simulations with the KF and GF convection schemes, with the latter being more skillful even at a grid spacing of 36 km in capturing the nocturnal timing that dominates in the Great Plains and North American monsoon region. Furthermore, the GF scheme exhibits much reduced sensitivity to model resolution compared to the KF scheme, consistent with the smoother transition from convective to large-scale (resolved) precipitation as horizontal resolution increases (Figure 11b). *Grell and Freitas* [2014] noted a similar behavior in the GF scheme applied to simulations over South America and attributed the smooth transition to the Arakawa's adjustment factor for estimating the fractional coverage of updraft and downdraft plumes [*Arakawa et al*., 2011] implemented in the GF scheme. As the model grid spacing approaches a few kilometers, the heating and drying rates produced by the GF scheme diminish [*Grell and Freitas*, 2014]. Consistently, we find that the GF scheme at 4 km is almost completely turned off, so precipitation is produced mainly by the resolved processes and the cloud tops become shallower (Figure 10) and more comparable to simulations at the same grid spacing, but without a convective parameterization. The GF scale-aware parameterization is being tested in the Model for Prediction Across Scales [*Skamarock et al*., 2012] global variable resolution modeling framework for convection-permitting simulations by using regional refinement.

Leung and Gao [2016] further analyzed the WRF simulations presented in this study, with a focus on land-atmosphere interactions. They found that simulations with the KF scheme at 36 km and 12 km grid spacing produce peak rainfall in the afternoon over both wet and dry soils. In contrast, at 4 km without a cumulus scheme, the model depicts a dominance of nocturnal and afternoon rain occurring preferentially over wet soil and dry soils, respectively. This suggests that land-atmosphere interactions are simulated differently in the 36 km/12 km simulations and the convection-permitting simulation, with the former featuring precipitation generated primarily in the afternoon through coevolution of convection with surface fluxes and PBL processes, while in the latter, wet soil moisture may be a response to the nocturnal rainfall that plays a more minor role in precipitation through feedback except over a longer time scale. With the ability to distinguish processes that generate nocturnal versus afternoon rainfall, the convection-permitting simulation may allow the role of land-atmosphere interactions to be more realistically investigated.

With the improvements in simulating precipitation amount and diurnal variability, the conspicuous warm biases of 2–4°C over the Southern Great Plains in the coarser resolution simulations are reduced, but warm biases of smaller magnitudes remain. Using simulations where the model winds are nudged toward reanalysis, we show that the warm biases are partly due to large-scale circulation biases, which appear to be rather insensitive to model resolution. With nudging of the winds above the PBL toward observations, moisture transport from the Gulf of California is enhanced to increase moisture flux convergence over the Southern Great Plains. Despite the increased moisture supply, nudging has no impacts on the diurnal timing of precipitation simulated by the model, which is more dominantly controlled by the representation of convection that is sensitive to model resolution and convective parameterizations.

With advances in computing, convection-permitting climate simulations are becoming more feasible by using regional climate models and global variable resolution models. This study adds to the limited literature that documents convection-permitting climate simulations and the associated challenges and opportunities [*Prein et al*., 2015]. For regional and global variable resolution modeling that involves simulations across a wide range of resolutions through nesting or regional refinement with unstructured grids, a key challenge is modeling across the gray zone to convection-permitting resolutions. This study emphasizes the importance of parameterizing convection and the use of nonhydrostatic dynamics across grid spacings from 36 km to 4 km. Efforts to improve the scale awareness of convective parameterizations will likely yield further advances in the future. For example, a recent study has shown improved precipitation in high-resolution (1–10 km) simulations by using an updated KF scheme that introduces scale-aware parameterized cloud dynamics [*Zheng et al*., 2016], and other approaches are actively being pursued. Regional refinement techniques could also introduce uncertainties in modeling precipitation through their impacts on the large-scale circulation associated with downscaling and upscaling of processes [*Hagos et al*., 2013; *Sakaguchi et al*., 2015, 2016]. Besides model development to address the obvious deficiencies, numerical experiments to systematically compare modeling approaches and development of metrics and diagnostics may yield insights for future design of high-resolution climate simulations for actionable climate science in support of decision making.

Acknowledgments
All data and simulation output used in this study are archived at the National Energy Research Scientific Computing Center (NERSC) and can be accessed by contacting L. Ruby Leung (ruby.leung@pnnl.gov). This study is supported by the U.S. Department of Energy Office of Science Biological and Environmental Research (BER) as part of the Regional and Global Climate Modeling Program. The brightness temperature was obtained from the CLAUS archive held at the British Atmospheric Data Centre, produced by using ISCCP source data distributed by the NASA Langley Data Center. We would like to thank Baijun Tian at Jet Propulsion Laboratory, California Institute of Technology, for the helpful discussions on the Fourier analysis of diurnal temperature. This research used computational resources from NERSC, a DOE User Facility supported by the Office of Science under contract DE-AC02-05CH11231. Additional computational resources were provided by the Pacific Northwest National Laboratory (PNNL) Institutional Computing program. PNNL is operated for DOE by Battelle Memorial Institute under contract DE-AC05-76RL01830.

References

Arakawa, A., J. H. Jung, and C. M. Wu (2011), Toward unification of the multiscale modeling of the atmosphere, *Atmos. Chem. Phys.*, *11*(8), 3731–3742.

Bacmeister, J. T., M. F. Wehner, R. B. Neale, A. Gettelman, C. Hannay, P. H. Lauritzen, J. M. Caron, and J. E. Truesdale (2014), Exploratory high-resolution climate simulations using the Community Atmosphere Model (CAM), *J. Clim.*, *27*(9), 3073–3099.

Ban, N., J. Schmidli, and C. Schär (2014), Evaluation of the convection-resolving regional climate modeling approach in decade-long simulations, *J. Geophys. Res. Atmos.*, *119*, 7889–7907, doi:10.1002/2014JD021478.

Ban, N., J. Schmidli, and C. Schär (2015), Heavy precipitation in a changing climate: Does short-term summer precipitation increase faster? *Geophys. Res. Lett.*, *42*, 1165–1172, doi:10.1002/2014GL062588.

Bechtold, P., N. Semane, P. Lopez, J.-P. Chaboureau, A. Beljaars, and N. Bormann (2014), Representing equilibrium and nonequilibrium convection in large-scale models, *J. Atmos. Sci.*, *71*(2), 734–753.

Carbone, R. E., J. D. Tuttle, D. A. Ahijevych, and S. B. Trier (2002), Inferences of predictability associated with warm season precipitation episodes, *J. Atmos. Sci.*, *59*(13), 2033–2056.

Chan, S. C., E. J. Kendon, H. J. Fowler, S. Blenkinsop, N. M. Roberts, and C. A. T. Ferro (2014), The value of high-resolution met office regional climate models in the simulation of multihourly precipitation extremes, *J. Clim.*, *27*(16), 6155–6174.

Chen, F., and J. Dudhia (2001), Coupling an advanced land surface-hydrology model with the Penn State-NCAR MM5 modeling system. Part I: Model implementation and sensitivity, *Mon. Weather Rev.*, *129*(4), 569–585.

Clark, A. J., W. A. Gallus, M. Xue, and F. Kong (2009), A comparison of precipitation forecast skill between small convection-allowing and large convection-parameterizing ensembles, *Weather Forecasting*, *24*(4), 1121–1140.

Dai, A., F. Giorgi, and K. E. Trenberth (1999), Observed and model-simulated diurnal cycles of precipitation over the contiguous United States, *J. Geophys. Res.*, *104*(D6), 6377–6402, doi:10.1029/98JD02720.

Daly, C., R. P. Neilson, and D. L. Phillips (1994), A statistical-topographic model for mapping climatological precipitation over mountainous terrain, *J. Appl. Meteorol.*, *33*(2), 140–158.

Davis, C. A., K. W. Manning, R. E. Carbone, S. B. Trier, and J. D. Tuttle (2003), Coherence of warm-season continental rainfall in numerical weather prediction models, *Mon. Weather Rev.*, *131*(11), 2667–2679.

Dirmeyer, P. A., et al. (2012), Simulating the diurnal cycle of rainfall in global climate models: Resolution versus parameterization, *Clim. Dyn.*, *39*(1), 399–418.

Dong, X., et al. (2011), Investigation of the 2006 drought and 2007 flood extremes at the Southern Great Plains through an integrative analysis of observations, *J. Geophys. Res.*, *116*, D03204, doi:10.1029/2010JD014776.

Ek, M. B., K. E. Mitchell, Y. Lin, E. Rogers, P. Grunmann, V. Koren, G. Gayno, and J. D. Tarpley (2003), Implementation of Noah land surface model advances in the National Centers for Environmental Prediction operational mesoscale Eta model, *J. Geophys. Res.*, *108*(D22), 8851, doi:10.1029/2002JD003296.

Fritsch, J. M., R. J. Kane, and C. R. Chelius (1986), The contribution of mesoscale convective weather systems to the warm-season precipitation in the United States, *J. Climate Appl. Meteorol.*, *25*(10), 1333–1345.

Gao, Y., J. S. Fu, J. B. Drake, Y. Liu, and J.-F. Lamarque (2012), Projected changes of extreme weather events in the eastern United States based on a high-resolution climate modeling system, *Environ. Res. Lett.*, *7*, 044025.

Grell, G. A. (1993), Prognostic evaluation of assumptions used by cumulus parameterizations, *Mon. Weather Rev.*, *121*(3), 764–787.

Grell, G. A., and D. Dévényi (2002), A generalized approach to parameterizing convection combining ensemble and data assimilation techniques, *Geophys. Res. Lett.*, *29*(14), 1693, doi:10.1029/2002GL015311.

Grell, G. A., and S. R. Freitas (2014), A scale and aerosol aware stochastic convective parameterization for weather and air quality modeling, *Atmos. Chem. Phys.*, *14*(10), 5233–5250.

Hagos, S., R. Leung, S. A. Rauscher, and T. Ringler (2013), Error characteristics of two grid refinement approaches in aquaplanet simulations: MPAS-A and WRF, *Mon. Weather Rev.*, *141*(9), 3022–3036.

Hodges, K. I., D. W. Chappell, G. J. Robinson, and G. Yang (2000), An improved algorithm for generating global window brightness temperatures from multiple satellite infrared imagery, *J. Atmos. Oceanic Technol.*, *17*(10), 1296–1312.

Hohenegger, C., and B. Stevens (2013), Controls on and impacts of the diurnal cycle of deep convective precipitation, *J. Adv. Model Earth Syst.*, *5*(4), 801–815, doi:10.1002/2012MS000216.

Hsu, K.-L., H. V. Gupta, X. Gao, and S. Sorooshian (1999), Estimation of physical variables from multichannel remotely sensed imagery using a neural network: Application to rainfall estimation, *Water Resour. Res.*, *35*(5), 1605–1618, doi:10.1029/1999WR900032.

Huffman, G. J., R. F. Adler, M. M. Morrissey, D. T. Bolvin, S. Curtis, R. Joyce, B. McGavock, and J. Susskind (2001), Global precipitation at one-degree daily resolution from multisatellite observations, *J. Hydrometeorol.*, *2*(1), 36–50.

Huffman, G. J., D. T. Bolvin, E. J. Nelkin, D. B. Wolff, R. F. Adler, G. Gu, Y. Hong, K. P. Bowman, and E. F. Stocker (2007), The TRMM multisatellite precipitation analysis (TMPA): Quasi-global, multiyear, combined-sensor precipitation estimates at fine scales, *J. Hydrometeorol.*, *8*(1), 38–55.

Hughes, M., and A. Hall (2010), Local and synoptic mechanisms causing Southern California's Santa Ana winds, *Clim. Dyn.*, *34*(6), 847–857.

Hughes, M., A. Hall, and R. G. Fovell (2007), Dynamical controls on the diurnal cycle of temperature in complex topography, *Clim. Dyn.*, *29*(2), 277–292.

Iacono, M. J., J. S. Delamere, E. J. Mlawer, M. W. Shephard, S. A. Clough, and W. D. Collins (2008), Radiative forcing by long-lived greenhouse gases: Calculations with the AER radiative transfer models, *J. Geophys. Res.*, *113*, D13103, doi:10.1029/2008JD009944.

Janjić, Z. I. (1990), The step-mountain coordinate: Physical package, *Mon. Weather Rev.*, *118*(7), 1429–1443.

Janjić, Z. I., J. P. Gerrity, and S. Nickovic (2001), An alternative approach to nonhydrostatic modeling, *Mon. Weather Rev.*, *129*(5), 1164–1178.
Jankov, I., W. A. Gallus, M. Segal, B. Shaw, and S. E. Koch (2005), The impact of different WRF model physical parameterizations and their interactions on warm season MCS rainfall, *Weather Forecasting*, *20*(6), 1048–1060.
Jin, E. K., I.-J. Choi, S.-Y. Kim, and J.-Y. Han (2016), Impact of model resolution on the simulation of diurnal variations of precipitation over East Asia, *J. Geophys. Res. Atmos.*, *121*, 1652–1670, doi:10.1002/2015JD023948.
Kain, J. S. (2004), The Kain-Fritsch convective parameterization: An update, *J. Appl. Meteorol.*, *43*(1), 170–181.
Kendon, E. J., N. M. Roberts, C. A. Senior, and M. J. Roberts (2012), Realism of rainfall in a very high-resolution regional climate model, *J. Clim.*, *25*(17), 5791–5806.
Klein, S. A., X. Jiang, J. Boyle, S. Malyshev, and S. Xie (2006), Diagnosis of the summertime warm and dry bias over the U.S. Southern Great Plains in the GFDL climate model using a weather forecasting approach, *Geophys. Res. Lett.*, *33*, L18805, doi:10.1029/2006GL027567.
Koo, M.-S., and S.-Y. Hong (2010), Diurnal variations of simulated precipitation over East Asia in two regional climate models, *J. Geophys. Res.*, *115*, D05105, doi:10.1029/2009JD012574.
Kuo, H. L. (1974), Further studies of the parameterization of the influence of cumulus convection on large-scale flow, *J. Atmos. Sci.*, *31*(5), 1232–1240.
Lebassi-Habtezion, B., and N. S. Diffenbaugh (2013), Nonhydrostatic nested climate modeling: A case study of the 2010 summer season over the western United States, *J. Geophys. Res. Atmos.*, *118*, 10,944–10,962, doi:10.1002/jgrd.50773.
Leung, L. R., and Y. Gao (2016), Regional downscaling of S2S prediction: Past lessons and future prospects, *CLIVAR Var.*, *14*(4), 13–17.
Leung, L. R., and Y. Qian (2003), The sensitivity of precipitation and snowpack simulations to model resolution via nesting in regions of complex terrain, *J. Hydrometeorol.*, *4*(6), 1025–1043.
Leung, L. R., and S. J. Ghan (1999), Pacific Northwest climate sensitivity simulated by a regional climate model driven by a GCM. Part I: Control simulations, *J. Clim.*, *12*(7), 2010–2030.
Leung, L. R., Y. Qian, and X. Bian (2003), Hydroclimate of the western United States based on observations and regional climate simulation of 1981–2000. Part I: Seasonal statistics, *J. Clim.*, *16*(12), 1892–1911.
Leung, L. R., Y. Qian, X. Bian, W. M. Washington, J. Han, and J. O. Roads (2004), Mid-century ensemble regional climate change scenarios for the western United States, *Clim. Change*, *62*(1), 75–113.
Liang, X.-Z., L. Li, A. Dai, and K. E. Kunkel (2004), Regional climate model simulation of summer precipitation diurnal cycle over the United States, *Geophys. Res. Lett.*, *31*, L24208, doi:10.1029/2004GL021054.
Ma, L.-M., and Z.-M. Tan (2009), Improving the behavior of the cumulus parameterization for tropical cyclone prediction: Convection trigger, *Atmos. Res.*, *92*(2), 190–211.
Maurer, E. P., A. W. Wood, J. C. Adam, D. P. Lettenmaier, and B. Nijssen (2002), A long-term hydrologically based dataset of land surface fluxes and states for the conterminous United States*, *J. Clim.*, *15*(22), 3237–3251.
Mearns, L. O., D. P. Lettenmaier, and S. McGinnis (2015), Uses of results of regional climate model experiments for impacts and adaptation studies: The example of NARCCAP, *Curr. Clim. Change Rep.*, *1*(1), 1–9.
Mellor, G. L., and T. Yamada (1982), Development of a turbulence closure-model for geophysical fluid problems, *Rev. Geophys.*, *20*(4), 851–875, doi:10.1029/RG020i004p00851.
Mesinger, F., et al. (2006), North American regional reanalysis, *Bull. Am. Meteorol. Soc.*, *87*(3), 343–360.
Morcrette, J. J., H. W. Barker, J. N. S. Cole, M. J. Iacono, and R. Pincus (2008), Impact of a new radiation package, McRad, in the ECMWF integrated forecasting system, *Mon. Weather Rev.*, *136*(12), 4773–4798.
Morrison, H., G. Thompson, and V. Tatarskii (2009), Impact of cloud microphysics on the development of trailing stratiform precipitation in a simulated squall line: Comparison of one- and two-moment schemes, *Mon. Weather Rev.*, *137*(3), 991–1007.
Nesbitt, S. W., R. Cifelli, and S. A. Rutledge (2006), Storm morphology and rainfall characteristics of TRMM precipitation features, *Mon. Weather Rev.*, *134*(10), 2702–2721.
Prein, A. F., et al. (2015), A review on regional convection-permitting climate modeling: Demonstrations, prospects, and challenges, *Rev. Geophys.*, *53*, 323–361, doi:10.1002/2014RG000475.
Prein, A. F., et al. (2017), The future intensification of hourly precipitation extremes, *Nat. Clim. Change*, *7*, 48–52, doi:10.1038/nclimate3168.
Rasmussen, R., et al. (2011), High-resolution coupled climate runoff simulations of seasonal snowfall over Colorado: A process study of current and warmer climate, *J. Clim.*, *24*(12), 3015–3048.
Sakaguchi, K., L. R. Leung, C. Zhao, Q. Yang, J. Lu, S. Hagos, S. A. Rauscher, L. Dong, T. D. Ringler, and P. H. Lauritzen (2015), Exploring a multiresolution approach using AMIP simulations, *J. Clim.*, *28*(14), 5549–5574.
Sakaguchi, K., J. Lu, L. R. Leung, C. Zhao, Y. Li, and S. Hagos (2016), Sources and pathways of the upscale effects on the Southern Hemisphere jet in MPAS-CAM4 variable-resolution simulations, *J. Adv. Model Earth Syst.*, *8*, 1786–1805, doi:10.1002/2016MS000743.
Seager, R., N. Naik, and G. A. Vecchi (2010), Thermodynamic and dynamic mechanisms for large-scale changes in the hydrological cycle in response to global warming, *J. Clim.*, *23*(17), 4651–4668.
Shin, H. H., and S.-Y. Hong (2013), Analysis of resolved and parameterized vertical transports in convective boundary layers at gray-zone resolutions, *J. Atmos. Sci.*, *70*(10), 3248–3261.
Skamarock, W. C., J. B. Klemp, J. Dudhia, D. O. Gill, D. M. Barker, M. G. Duda, X. Huang, W. Wang, and J. G. Powers (2008), A description of the advanced research WRF version 3, *NCAR Tech. Note, NCAR/TN-475 + STR*, 8 pp., Natl. Cent. for Atmos. Res., Boulder, Colo. [Available at http://www.mmm.ucar. edu/wrf/users/docs/arw v3.pdf, 2008.]
Skamarock, W. C., J. B. Klemp, M. G. Duda, L. D. Fowler, S.-H. Park, and T. D. Ringler (2012), A multiscale nonhydrostatic atmospheric model using centroidal voronoi tessellations and C-grid staggering, *Mon. Weather Rev.*, *140*(9), 3090–3105.
Sorooshian, S., K.-L. Hsu, X. Gao, H. V. Gupta, B. Imam, and D. Braithwaite (2000), Evaluation of PERSIANN system satellite-based estimates of tropical rainfall, *Bull. Am. Meteorol. Soc.*, *81*(9), 2035–2046.
Stauffer, D. R., and N. L. Seaman (1990), Use of four-dimensional data assimilation in a limited-area mesoscale model. Part I: Experiments with synoptic-scale data, *Mon. Weather Rev.*, *118*(6), 1250–1277.
Taylor, K. E. (2001), Summarizing multiple aspects of model performance in a single diagram, *J. Geophys. Res.*, *106*(D7), 7183–7192, doi:10.1029/2000JD900719.
Tian, B., I. M. Held, N.-C. Lau, and B. J. Soden (2005), Diurnal cycle of summertime deep convection over North America: A satellite perspective, *J. Geophys. Res.*, *110*, D08108, doi:10.1029/2004JD005275.
von Storch, H., H. Langenberg, and F. Feser (2000), A spectral nudging technique for dynamical downscaling purposes, *Mon. Weather Rev.*, *128*(10), 3664–3673.
Waldron, K. M., J. Paegle, and J. D. Horel (1996), Sensitivity of a spectrally filtered and nudged limited-area model to outer model options, *Mon. Weather Rev.*, *124*(3), 529–547.

Wang, Y.-Q., L. R. Leung, J. L. McGregor, D.-K. Lee, W.-C. Wang, Y. Ding, and F. Kimura (2004), Regional climate modeling: Progress, challenges, and prospects, *J. Meteorol. Soc. Jpn.*, *82*(6), 1599–1628.

Xia, Y., et al. (2012a), Continental-scale water and energy flux analysis and validation for North American Land Data Assimilation System project phase 2 (NLDAS-2): 2. Validation of model-simulated streamflow, *J. Geophys. Res.*, *117*, D03110, doi:10.1029/2011JD016051.

Xia, Y., et al. (2012b), Continental-scale water and energy flux analysis and validation for the North American Land Data Assimilation System project phase 2 (NLDAS-2): 1. Intercomparison and application of model products, *J. Geophys. Res.*, *117*, D03109, doi:10.1029/2011JD016048.

Yang, G.-Y., and J. Slingo (2001), The diurnal cycle in the tropics, *Mon. Weather Rev.*, *129*(4), 784–801.

Yang, Q., L. R. Leung, J. Lu, Y.-L. Lin, S. Hagos, K. Sakaguchi, and Y. Gao (2017), Exploring the effects of a non hydrostatic dynamical core in high-resolution aquaplanet simulations, *J. Geophys. Res. Atmos.*, doi:10.1002/2016JD025287.

Zhang, G. J., and N. A. McFarlane (1995), Sensitivity of climate simulations to the parameterization of cumulus convection in the Canadian climate centre general circulation model, *Atmos. Ocean*, *33*(3), 407–446.

Zhang, Y., V. Dulière, P. W. Mote, and E. P. Salathé (2009), Evaluation of WRF and HadRM mesoscale climate simulations over the U.S. Pacific Northwest, *J. Clim.*, *22*(20), 5511–5526.

Zheng, Y., K. Alapaty, J. A. Herwehe, A. D. Del Genio, and D. Niyogi (2016), Improving high-resolution weather forecasts using the Weather Research and Forecasting (WRF) model with an updated Kain-Fritsch scheme, *Mon. Weather Rev.*, 833–860.

Erratum

The original version of this article was published without the supporting information. The supporting information is included, and this version may be considered the authoritative version of record.